energies

MDPI

Article

Multiphysics Measurements for Detection of Gas Hydrate Formation in Undersaturated Oil Coreflooding Experiments with Seawater Injection

Bianca L. S. Geranutti , Mathias Pohl , Daniel Rathmaier , Somayeh Karimi and Manika Prasad and Luis E. Zerpa *

Center for Rock and Fluid Multiphysics, Colorado School of Mines, Golden, CO 80401, USA; drathmaier@mines.edu (D.R.); mprasad@mines.edu (M.P.)
* Correspondence: lzerpa@mines.edu; Tel.: +1-303-384-2627

Abstract: A solid phase of natural gas hydrates can form from dissolved gas in oil during cold water injection into shallow undersaturated oil reservoirs. This creates significant risks to oil production due to potential permeability reduction and flow assurance issues. Understanding the conditions under which gas hydrates form and their impact on reservoir properties is important for optimizing oil recovery processes and ensuring the safe and efficient operation of oil reservoirs subject to waterflooding. In this work, we present two fluid displacement experiments under temperature control using Bentheimer sandstone core samples. A large diameter core sample of 3 inches in diameter and 10 inches in length was instrumented with multiphysics sensors (i.e., ultrasonic, electrical conductivity, strain, and temperature) to detect the onset of hydrate formation during cooling/injection steps. A small diameter core sample of 1.5 inches in diameter and 12 inches in length was used in a coreflooding apparatus with high-precision pressure transducers to determine the effect of hydrate formation on rock permeability. The fluid phase transition to solid hydrate phase was detected during the displacement of live-oil with injected water. The experimental procedure consisted of cooling and injection steps. Gas hydrate formation was detected from ultrasonic measurements at 7 °C, while strain measurements registered changes at 4 °C after gas hydrate concentration increased further. Ultrasonic velocities indicated the pore-filling morphology of gas hydrates, resulting in a high hydrate saturation of theoretically up to 38% and a substantial risk of intrinsic permeability reduction in the reservoir rock due to pore blockage by hydrates.

Keywords: gas hydrate; multiphysics measurements; acoustics; monitoring; rock physics; saturation estimation

check for updates

Citation: Geranutti, B.L.S.; Pohl, M.; Rathmaier, D.; Karimi, S.; Prasad, M.; Zerpa, L.E. Multiphysics Measurements for Detection of Gas Hydrate Formation in Undersaturated Oil Coreflooding Experiments with Seawater Injection. *Energies* **2024**, *17*, 3280. https://doi.org/10.3390/en17133280

Academic Editors: Lunxiang Zhang and Hongsheng Dong

Received: 5 June 2024
Revised: 18 June 2024
Accepted: 27 June 2024
Published: 4 July 2024

Copyright: © 2024 by the authors. Licensee MDPI, Basel, Switzerland. This article is an open access article distributed under the terms and conditions of the Creative Commons Attribution (CC BY) license (https://creativecommons.org/licenses/by/4.0/).

1. Introduction

Gas hydrates are crystalline solids formed by gas and water molecules at high pressures and low temperatures (typically above the ice point), where small gas molecules (between 0.35 and 0.9 nm) are trapped within the cavities of hydrogen-bonded water molecules. The trapped gas is in the size range between nitrogen and normal pentane [1,2]. Gas hydrates occur naturally onshore below the permafrost and at or below the seafloor within sediments [1]. This paper presents an experimental study of gas hydrate formation in undersaturated oil reservoirs during cold water injection, which could result in formation damage (i.e., permeability decrease by the formation of solid gas hydrate within the rock pore network). Normally, the temperature and pressure profiles of petroleum reservoirs are such that hydrates are not stable. However, in colder regions, conditions can be favorable for hydrate formation at the water-hydrocarbon interface [3,4].

In the literature, there are reported experimental studies connecting the reduction in rock permeability to hydrate concentration [5–10]. The permeability reduction is directly related to the gas hydrates' deposition morphology and rock properties. Previous work,

however, considered water and natural gas systems but most conventional commercial hydrocarbon reservoirs worldwide target the oil phase which requires at a certain stage of production some sort of secondary recovery mechanism, such as waterflooding. To the best of the authors' knowledge, looking at the multiphase problem of gas hydrate formation from the gaseous compounds entirely dissolved in the oil phase, has not yet been researched. Therefore, this work contributes to the understanding of gas hydrate formation in oil reservoirs during cold seawater injection. The physical properties of gas hydrate-bearing porous media depend on the volume fraction and spatial distribution of the hydrate phase. The grain size and the effective stress determine the hydrates' distribution in sediments [11].

There are two main morphologies for hydrate deposition in the pore space. The first one is when hydrates form along the grain surfaces. This type can only be seen in the contact of the grains (i.e., cementing) and enveloping the grain (i.e., grain/pore coating). In the second morphology, hydrates are initially deposited in the middle of the pores resulting in a pore-filling morphology [12,13]. When hydrates form as grain coating, changes in permeability are expected to be small. When hydrates form as pore filling, the permeability loss can be more severe with the potential of completely plugging the pore throats [5,9,10].

The hydrate morphology in sediments was connected to acoustic velocities in previous studies [12,14–17]. In both cases where gas hydrates are formed at the pore walls (i.e., grain/pore coating and cementing), P- and S-wave velocities increased with hydrate saturation. For pore-filling hydrates, the P-wave velocity increased while the S-wave velocity is practically independent of hydrate concentration [12].

Gas hydrates are also considered electrical insulators. Their formation replaces the conductive pore fluid, restricting the flow of electric current [18–21]. However, there is a competing effect due to the salinity increase in the remaining water in the pore space [22].

In this paper, we demonstrate experimental hydrate formation from an undersaturated oil reservoir using coreflooding experiments. Multiphysics measurements (ultrasonic, strain, and temperature) were implemented for the detection of fluid phase transitions into a solid phase (i.e., gas hydrates) and to investigate the distribution of gas hydrates inside the core.

2. Materials and Methods

The materials used in this research were two Bentheimer sandstone core samples, one of 3 inches in diameter and 10 inches in length (large diameter core, required for the installation sensors on the core), and the other of 1.5 inches in diameter and 12 inches in length (small diameter core, required for accurate pressure drop measurements). The fluid system consisted of synthetic formation water, seawater, and a recombined crude oil with synthetic gas to mimic a live-oil composition. The experimental procedure to assess hydrate formation consisted of cooling, injection, and multiphysics measurement steps.

2.1. Core Sample Preparation

The selected rock for the experiments was the Bentheimer sandstone provided by Kocurek Industries from the Valaginian formation. This sandstone is considered to be ideal for standard laboratory experiments because of its limited amount of minerals (with 91.7 wt% quartz, 4.9 wt% feldspars, 2.7 wt% clay minerals, 0.4 wt% carbonates, and 0.2 wt% pyrite and iron hydroxides), a constant grain size distribution, porosity, permeability, and dielectric values [23].

Kocurek Industries reported the average porosity of the Bentheimer to be between 23 and 26%, and the permeability between 1500 and 3000 mD. To check the porosity and permeability of Bentheimer samples for the pressures used in this study (8270 kPa to 13,790 kPa), a core plug sample (1.5 inches in diameter and 2 inches in length) was placed in the CMS-300 apparatus. The CMS-300 performs computer-controlled measurements of reservoir rock samples to determine pore volume and Klinkenberg permeability. The core sample was pressurized with helium and the measurements at experimental pressure conditions yielded a porosity of 25.5% and permeability of 2750 mD.

The first coreflooding test used a core sample of 3 inches in diameter and 10 inches in length, with an estimated pore volume of 290 mL. Four types of multiphysics sensors were installed on the core sample: 1 MHz piezo-electrical crystals (P- and S-wave for acoustic velocity measurements), conductivity electrode rings, 1000 Ohm strain gauges for deformation, and K-Type thermocouple sensors for temperature recording along the core. The core preparation consisted of the lateral isolation, made with K20 epoxy, to avoid leaks from the confining hydraulic oil into the core. Previous to the installation of the sensors, grooves were cut to create a contact area for the conductivity electrode rings. Figure 1 shows the core after the lateral isolation process and the core after the grooves were made.

Twelve strain gauges were installed, followed by the installation of nine electrode rings inside the grooves. The elastic wave crystals were prepared and tested before the installation on the core. In total, 40 crystals (20 P-waves and 20 S-waves) were installed along the core. The last sensors installed were 12 temperature sensors. Figure 2 shows the sensor installation steps of the core sample.

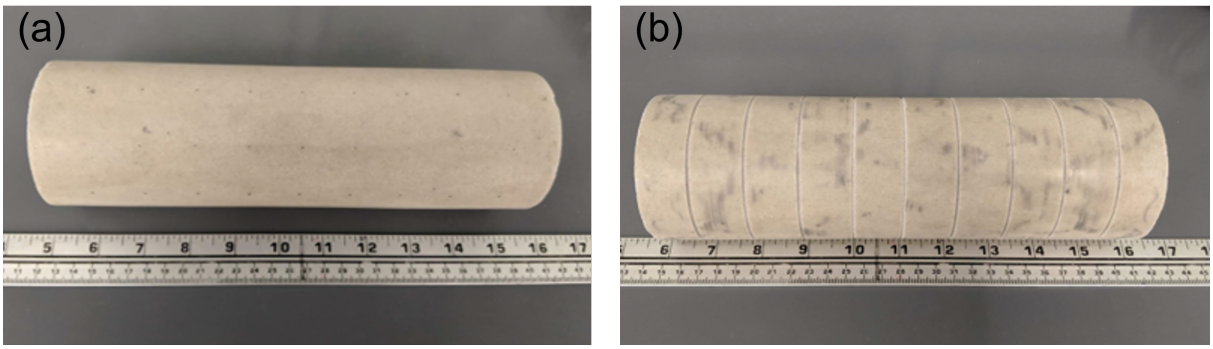


Figure 1. Core sample preparation. Lateral isolation with K20 epoxy in (**a**) and grooves creation for conductivity rings in (**b**).

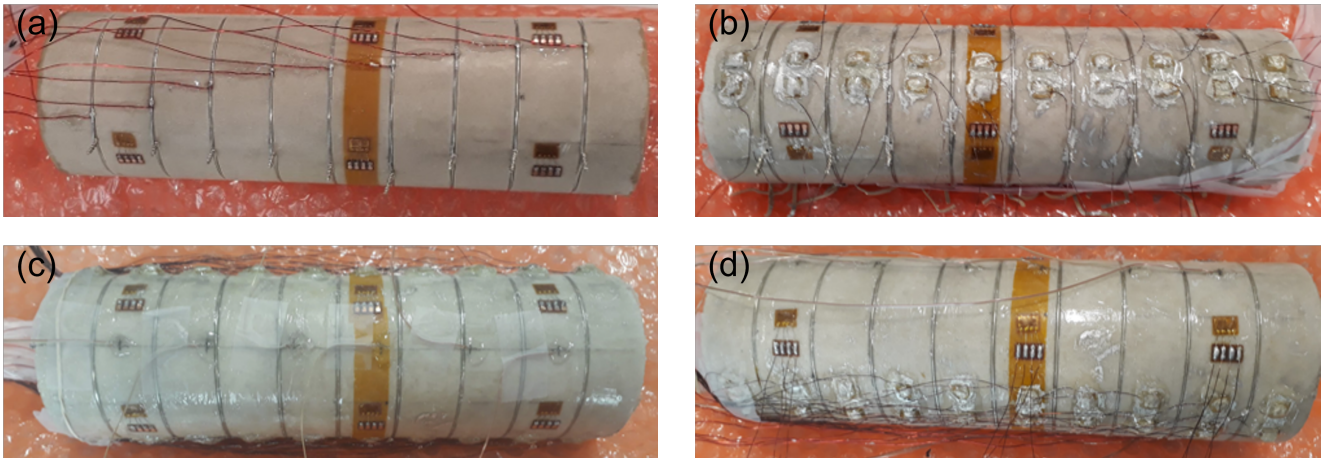


Figure 2. Sensor installation in the core sample: strain gauges and electrode rings installed in (**a**), wave crystals installed in (**b**), temperature sensors installed in (**c**), and all sensors finalized in (**d**).

The entire core was sandwiched between two end-caps that were glued onto the core. A PVC ring and a foil were installed on the bottom cap to create a void space to be filled with soft epoxy. The soft epoxy has the purpose of protecting the sensors from the confining hydraulic oil. Figure 3 shows the soft epoxy process.

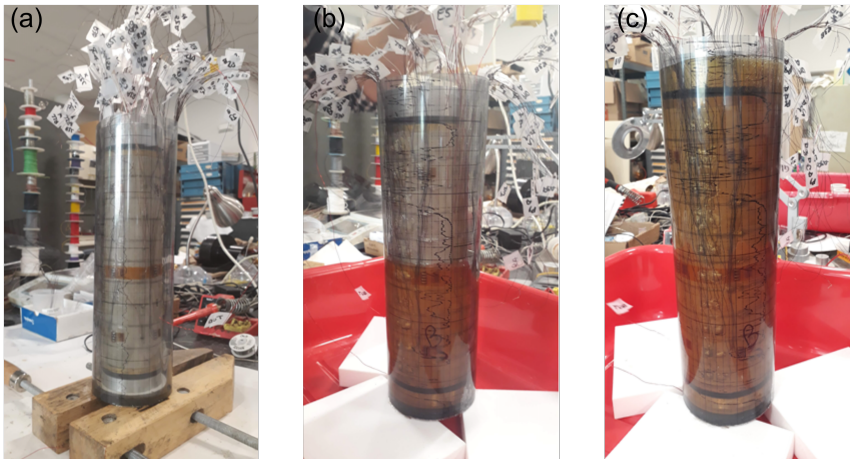


Figure 3. Soft epoxy process: PVC and foil was placed on the core in (**a**), followed by the soft epoxy deposition in (**b**), and finalized by the hardening of soft epoxy in (**c**).

2.2. Synthetic Fluids Preparation

Synthetic formation brine and seawater were prepared using the compositions presented in Table 1. The total salinity was 74.6 g/L for the formation water and 39.3 g/L for the seawater.

Table 1. Composition of the synthetic formation water and seawater used in the coreflood experiment. The core sample is initially fully saturated with formation water before displacement by live-oil (drainage), and seawater is used for the subsequent coreflood to represent waterflooding displacing the oil (imbibition).

Salt Types	Formation Water Composition (g/L)	Seawater Composition (g/L)
NaCl	56.930	25.690
$MgCl_2 \cdot 6H_2O$	8.450	11.040
$CaCl_2 \cdot 2H_2O$	7.250	1.560
$SrCl_2 \cdot 6H_2O$	0.736	0.024
$BaCl_2 \cdot 2H_2O$	0.697	-
KCl	0.243	0.784
$NaBO_2 \cdot 4H_2O$	0.043	0.201
Na_2SO_4	0.030	-

A dead oil sample with a gravity of 38.3 °API and a viscosity of 2.45 cp was recombined with a synthetic gas mixture to mimic an undersaturated oil reservoir. The composition of the natural gas is presented in Table 2. The live-oil preparation occurred in the PVT 400/1000 Analysis System from Sanchez technologies by mixing the dead oil with the synthetic gas. The first step was to inject the dead oil at atmospheric pressure and initial experimental temperature (17 °C) into the cell. The second step was the pressurization of the cell to the experimental pressure (8270 kPa), followed by the injection of synthetic gas. The oil–gas mixture was pressurized to 13,790 kPa for 24 h to allow for the gas to completely dissolve into the oil phase. The measured bubble point of the live-oil was 7580 kPa.

Table 2. Composition of synthetic gas mixture used for live-oil recombination.

Component	Composition (mol%)
CO_2	7.0
CH_4	80.0
C_2H_6	7.0
C_3H_8	4.0
C_4H_{10}	2.0

2.3. Experimental Procedure for the Large Core

Figure 4 shows the coreflooding setup designed for the large diameter core with the physical dimensions of 3 inches in diameter and 10 inches in length. The pressure vessel was vertically placed in a barrel for temperature isolation. The vessel was surrounded by a copper coil that was connected to the recirculating chiller for temperature control. Three Teledyne 500D ISCO pumps (Teledyne ISCO Inc., Lincoln, NE, USA) were incorporated in this setup providing the net confining stress, the pore pressure backup, and for fluid injection. Four types of data acquisition were planned for this setup: (1) elastic waves were generated using a pulser and measured with Tektronix TDS 3014C oscilloscope (Tektronix Inc., Beaverton, OR, USA), (2) complex conductivities were measured with the SIP-Lab from Radic Research (Radic Research, Berlin, Germany), (3) static deformation, and (4) temperature measured continuously. Before saturating the core with formation water, a vacuum was applied to the entire core (using a Fisher Scientific PU1309-N840.0-9.01 vacuum pump from Fisher Scientific International, Inc., Hampton, NH, USA).

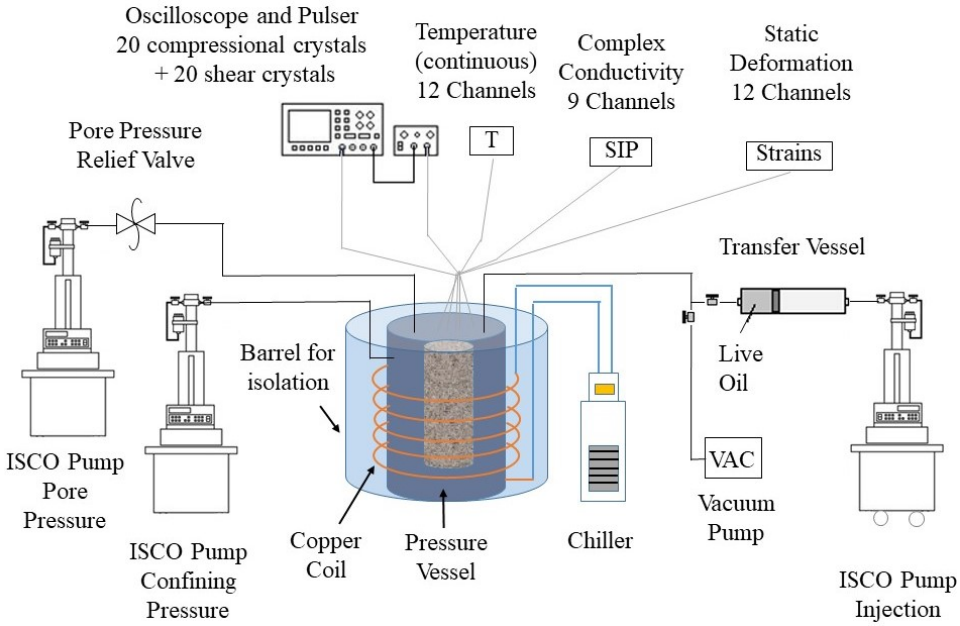


Figure 4. Coreflood setup constituted of a pressure vessel, vacuum pump, three ISCO pumps, chiller, and data acquisition equipment.

The coreflooding experiment was performed at constant pore pressure of 8270 kPa and a net confining stress of 15,270 kPa. Initially, the core was fully saturated with formation water. Then, three pore volumes of live-oil were injected to displace the formation water to irreducible water saturation. The hydrate detection procedure consisted of a series of cooling steps with an injection period, followed by multiphysics measurements. For the cooling steps, the temperature was set to 15, 12, 10, 8, 7, 6, 4, 3, and 2 °C, respectively. Each cooling step was represented by a cooling period and temperature stabilization for 24 h, followed by seawater injection from the bottom of the sample at a volumetric rate of 0.2 cm^3/min. The formation of hydrates within the core is expected to increase P-wave as well as S-wave velocity measurements depending on the hydrate deposition morphology, i.e., whether hydrates will become load bearing or remain in the center of the pores. Furthermore, and because of hydrates exhibit a volume expansion upon formation, it is expected that the in situ formation of hydrates causes a deformation of the core.

For the ultrasonic measurements, each P-wave crystal was paired up with a S-wave crystal. Each pair was separated by 1 inch with the following pair along the core length. The signal was transmitted from one crystal (P or S) to another one of the respective crystals across the diameter of the sample (180°). The standard deviation for the velocities among

the crystals was around 30 m/s. The measurement error was determined at 1% for the P-waves and 3% for the S-waves.

Omega SGT-3/1000-XY11 strain gauges (Omega Engineering, Inc., Norwalk, CT, USA) were used for deformation measurements across the core length. Each strain gauge had two strain directions: horizontal and vertical. The measurements of the effective strain were calculated by Wheatstone bridge circuit voltages recorded by a computer with MCC DAQ software version 4.2.1 (Measurement Computing, Norton, MA, USA). The main purpose of strain measurements was to evaluate the possible expansion of the rock due to gas hydrate formation. Similarly to deformation, the temperature sensors were placed along the whole length of the core. The temperature sensors were connected to KTA-259K thermocouple shields that passed the information to the Mega 2560 R3 Arduino boards (Arduino, Ivrea, Italy) controlled by a computer with the Arduino IDE software version 2.3.2. The temperature was recorded by the CoolTerm application from Roger Meier. The temperature sensors measured the temperature across the core and provided supporting information during gas hydrate formation as it is an exothermic reaction [2].

2.4. Experimental Procedure for the Small Core

Figure 5 shows the coreflooding setup designed for the small diameter core with the physical dimensions of 1.5 inches in diameter and 12 inches in length. The pressure vessel setup including the chiller for temperature control and pumps for pore and confining pressure, respectively, was similar to the experimental procedure for the large core. In addition, pressure gauges of the type Omega DPG210-5K (Omega Engineering, Inc., Norwalk, CT, USA) with an accuracy of 0.1% and a pressure range from 0 to 5000 psig, and a differential pressure transducer of the type Omega PX3005-25 (Omega Engineering, Inc., Norwalk, CT, USA) with an accuracy of 0.075% and a pressure range from −1.0 to 1.0 psi, measure the differential pressure between the top and the bottom of the core. This measured differential pressure gives indirect information about the formation of hydrates within the porous media of the sample as hydrates clog the pore channels which increases the resistance to fluid flow and manifests in a higher differential pressure.

The coreflooding experiment followed the same procedure as for the large core with the adjustment of temperature cooling steps to 15, 11, 8, 7, 6, 5, 4, 3, and 2 °C, and a volumetric injection rate to 0.05 cm^3/min.

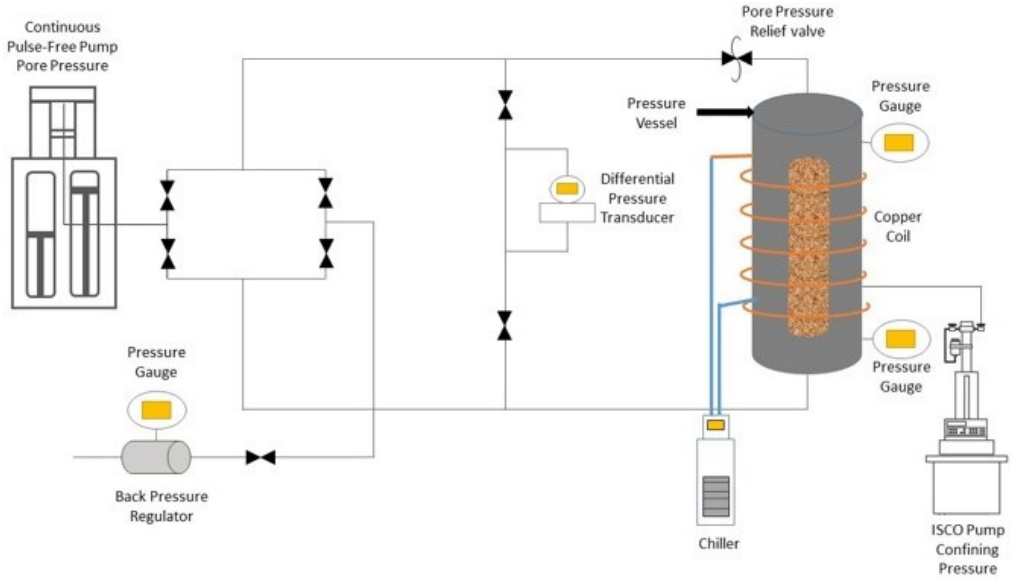


Figure 5. Coreflood setup constituted of a pressure vessel, differential pressure transducer, pressure gauges, ISCO pump, continuous pulse-free pump, chiller, and back pressure regulator.

3. Results

Before performing the coreflooding experiment to detect hydrate formation with multiphysics measurements, we calculated the hydrate equilibrium conditions in terms of pressure and temperature for different water salinities (i.e., fresh water, seawater, and formation water). We performed these calculations with the software PVTSim Nova version 5.1 (Calsep A/S, Copenhagen, Denmark) using the synthetic live-oil and water compositions with varying salinities as input parameters and the Peng–Robinson (PR) Peneloux Equation of State (EOS). Figure 6 shows the calculated hydrate equilibrium curves. The region to the right of the curves, at higher temperatures and lower pressures, represent conditions were gas hydrates are not stable while the region to the left of the curves represents the hydrate stable conditions. The increase in water salinity shifts the hydrate equilibrium conditions to lower temperatures.

During a cooling process that takes a hydrocarbon water system below the hydrate equilibrium temperature, there will be a phase transition into a solid hydrate phase which begins with the nucleation of a hydrate crystal. Hydrate nucleation requires several degrees of subcooling below the equilibrium temperature. It is expected that hydrates will start to form when the system is several degrees colder than the calculated hydrate equilibrium temperature. For the system considered in this work, the hydrate equilibrium temperature is 11 °C for the salinity of formation water.

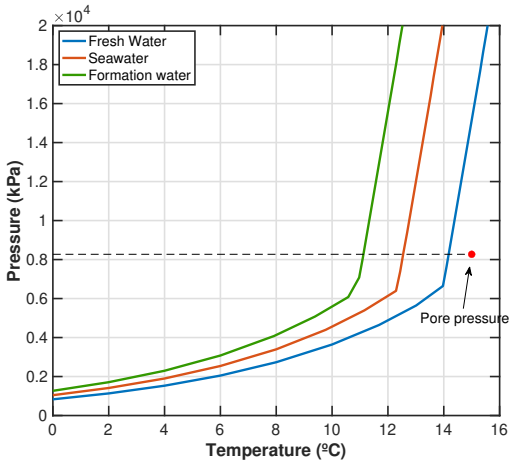


Figure 6. Hydrate equilibrium curves for fresh water, seawater, and formation water, indicating the initial experiment pressure and temperature conditions

3.1. Large Diameter Core Sample Results

The formation of a solid gas hydrate phase was detected by changes in the arrival time of elastic waves. Initially, no significant changes in elastic waves were observed during cooling steps from 15 to 8 °C. A small decrease in the P-wave arrival time was noticed at the bottom of the sample due to an increase in water saturation because of oil displacement by seawater. Changes in amplitude were visible in the raw data, however, the arrival time was very similar. The waterfront was visible at the P4 crystal (fourth acoustic crystal location from the top to the bottom of the sample) for the 8 °C seawater injection step. There was no significant change in the S-waves. The period of injection was reduced from 60 min to 20 min at the same injection rate (0.2 cm^3/min) for the following cooling steps to maintain a sufficient amount of live-oil in the sample.

Significant changes in the arrival time of elastic waves due to gas hydrate formation were observed between 8 and 7 °C. Figure 7 shows the raw P- and S-waves measured for the 8 and 7 °C seawater injection steps for representative crystals at the top (P1), middle (P5), and bottom (P10) of the core sample. It is possible to see a decrease in the P-wave arrival time for the 7 °C curves at the three representative locations (P1, P5, and P10). The S-waves were slightly affected at 7 °C, but the difference remained inside the error margin of the

measurements. The S-wave in the middle of the core was the least affected, probably because of a lower oil saturation due to a water imbibition effect. The following cooling steps had the purpose of evaluating hydrate growth. For the following steps, the P-wave arrival time kept decreasing.

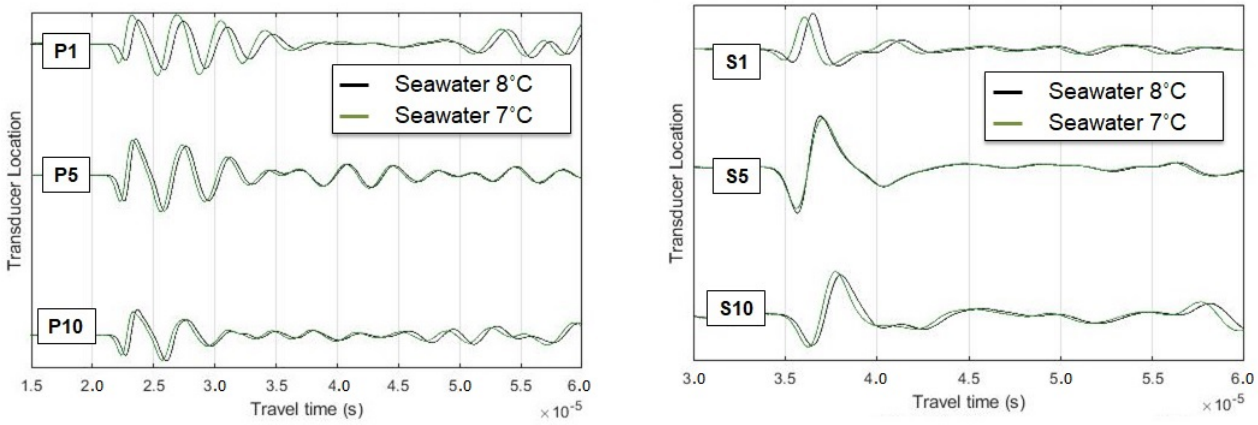


Figure 7. Raw P-waves (**left**) and S-waves (**right**) comparison for seawater injection at 8 °C and seawater injection at 7 °C indicating gas hydrate formation.

The acoustic velocities were calculated based on the arrival time and sample dimensions. No delay time was considered as the crystals were glued directly onto the sample surface. A linear temperature correction to remove temperature effects was performed based on previous results from the evaluation of temperature effects with a water-saturated core [24]. Figure 8 shows the P- and S-wave velocities measured at transducers along the length of the core for conditions before injection and for cooling/injection steps at 8 °C, 7 °C, and 4 °C. From before seawater injection to 8 °C, an increase in P-wave velocity in the bottom part (P7 to P10) of the sample due to an increase in water saturation was observed. The velocity increase due to water injection was in the order of 10 to 20 m/s, which are smaller than the error margin.

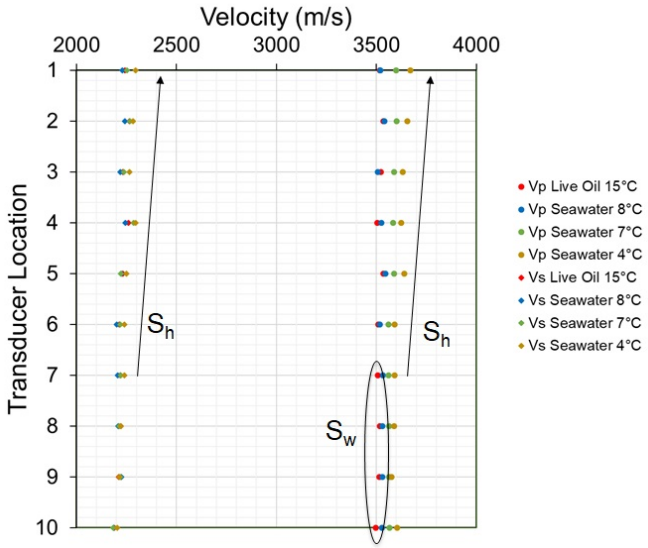


Figure 8. P- and S-wave velocities for each crystal position of the large core sample at 15, 8, 7, and 4 °C. P-wave velocity increase was greater at the top of the sample due to a higher dissolved gas availability to form gas hydrate.

From 8 °C to 7 °C, the P-wave velocity increased all over the sample indicating hydrate formation. The top crystal showed a higher increase, approximately 80 m/s. The bottom crystal had a smaller increase, approximately 40 m/s, associated also with a greater water saturation. The S-wave velocity increase, even in the top portion, was smaller than the error margin, approximately 20 m/s. As a solid phase, gas hydrates increase the compressional wave velocity propagation, as observed in P-wave velocities. The same does not happen for S-waves because a water film exists between the rock surface and hydrates (i.e., in a pore-filling hydrate morphology), which does not allow the S-wave to be transmitted. The velocity increase is higher in the top portion (P1 to P7) because of the availability of more dissolved gas (i.e., higher oil saturation towards the top of the core sample) leads to more hydrate formation. From 7 °C to 4 °C, the P-wave velocity increased all over the sample indicating the formation of additional gas hydrates. The top acoustic crystal showed a higher increase, approximately 70 m/s. The bottom crystal was around 40 m/s. The S-wave velocity started to have a small impact on the top of the sample, approximately 40 m/s (close to the error margin).

Figure 9 shows the average P-wave velocity for every experimental procedure step. The average velocity increase due to water saturation increase was very small, around 5 m/s. From 8 °C to 7 °C, the average velocity increased 50 m/s, indicating the formation of gas hydrate. For lower temperatures, the velocity kept increasing due to additional hydrate formation with values between 10 and 30 m/s for each subsequent cooling step. Figure 10 shows the average S-wave velocity for every experimental procedure step. No significant change was observed due to an increase in water saturation or due to gas hydrate formation.

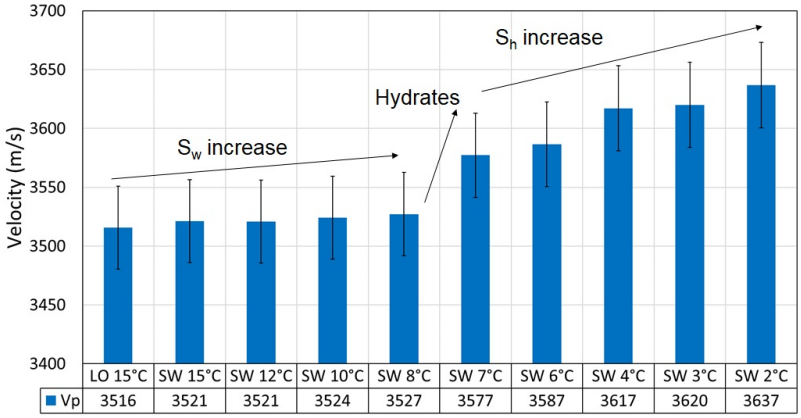


Figure 9. P-wave average velocities for hydrate detection experimental procedure. From 8 to 7 °C an increase in velocity indicated gas hydrate formation. Gas hydrates kept growing for lower temperatures.

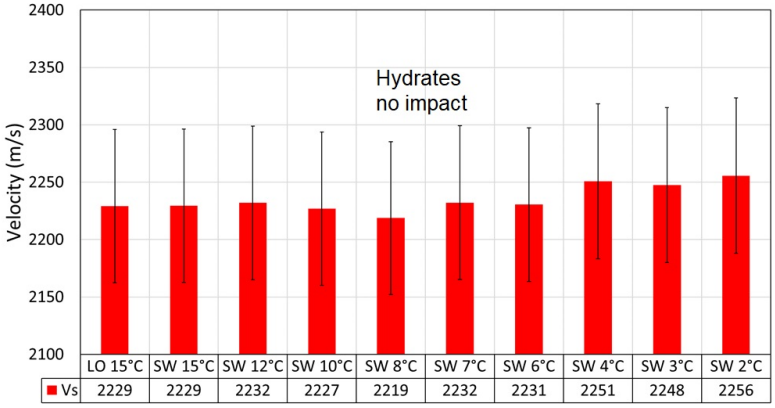
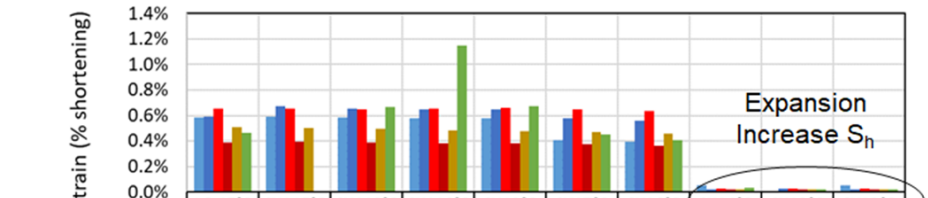


Figure 10. S-wave average velocities for hydrate detection experimental procedure. No significant change was observed.

Figure 11 shows the strain values for the gas hydrate experimental procedure. The readings were performed in two directions (vertical and horizontal) at three locations along the core (top, middle, and bottom). Only half of the strain gauges worked properly until the end of the procedure because of cable rupture problems. Bottom A-C vertical at 15 °C and Top B-D vertical at 3 °C presented values higher than 2% strain and were inconsistent with the other values, so these are not displayed. The reduction in strain was observed from 4 °C to 2 °C, indicating that the core sample expanded. Similar to ice, the transition of fluid phases into solid gas hydrates expand in volume [2]. The ultrasonic measurements show that 4 °C was the temperature at which hydrate saturation increased significantly in the core, so the strain measurements are in agreement with ultrasonic data.



	LO 15°C	SW 15°C	SW 12°C	SW 10°C	SW 8°C	SW 7°C	SW 6°C	SW 4°C	SW 3°C	SW 2°C
Top B-D vertical	0.6%	0.6%	0.6%	0.6%	0.6%	0.4%	0.4%	0.1%		0.1%
Top B-D horizontal	0.6%	0.7%	0.7%	0.6%	0.6%	0.6%	0.6%	0.0%	0.0%	0.0%
Middle B-D vertical	0.7%	0.7%	0.6%	0.7%	0.7%	0.7%	0.6%	0.0%	0.0%	0.0%
Middle B-D horizontal	0.4%	0.4%	0.4%	0.4%	0.4%	0.4%	0.4%	0.0%	0.0%	0.0%
Middle A-C vertical	0.5%	0.5%	0.5%	0.5%	0.5%	0.5%	0.5%	0.0%	0.0%	0.0%
Bottom A-C vertical	0.5%		0.7%	1.1%	0.7%	0.5%	0.4%	0.0%	0.0%	0.0%

Figure 11. Strain values for gas hydrate detection experimental procedure. Expansion of the core sample was notice at 4 ° C.

Figure 12 shows the temperature readings from 8 °C to 7 °C from the gas hydrate detection experimental procedure. The temperature was measured in opposite diameters (A and B) along the length of the core (1 at the top until 6 at the bottom). The increase in temperature due to the exothermic hydrate formation reaction was visible in the top to the middle portion of the sample (T1, T2, T3, and T4). The sensor T3A presented a reading issue, but a variation was noticed between 17 and 18 h. To maintain the temperature of the core sample the closest possible to the respective seawater injection step temperature, the cooler sometimes had the set temperature adjusted 4 h prior to the data acquisition. This happened and is observed for the 7 °C seawater injection step approximately at 20 h of the recorded data. The bottom part of the sample only had temperature fluctuations after this adjustment. In the bottom part, gas hydrate formation could not have been enough to increase the temperature or it happened simultaneously with the cooler adjustment. The room temperature was stable during the cooling. The Arduinos' temperatures represent the inside board temperature reading and were a few degrees higher than the room temperature.

Elastic waves and temperature measurements supported that gas hydrates formed at 7 °C. The strain and pressure differential showed significant hydrates impact at 4 °C. The P-waves and temperature were more sensitive to initial gas hydrates change, while the other measurements only detected or were affected by gas hydrates when the saturation increased.

The pressure differential between the injection ISCO pump (set to maintain a constant injection rate) and the backpressure ISCO pump (set to maintain a constant pressure) was recorded during the coreflood experiment. From 6 °C to 4 °C, an increase of 20 kPa pressure differential was noticed. The pressure differential increase could indicate resistance to flow due to gas hydrate saturation increase. ISCO pumps do not have a good precision to measure pressure differentials in temperature oscillating environments; therefore, another experiment with high-accuracy pressure gauges was performed to corroborate this hypothesis on the smaller core sample of the Bentheimer sandstone outcrop.

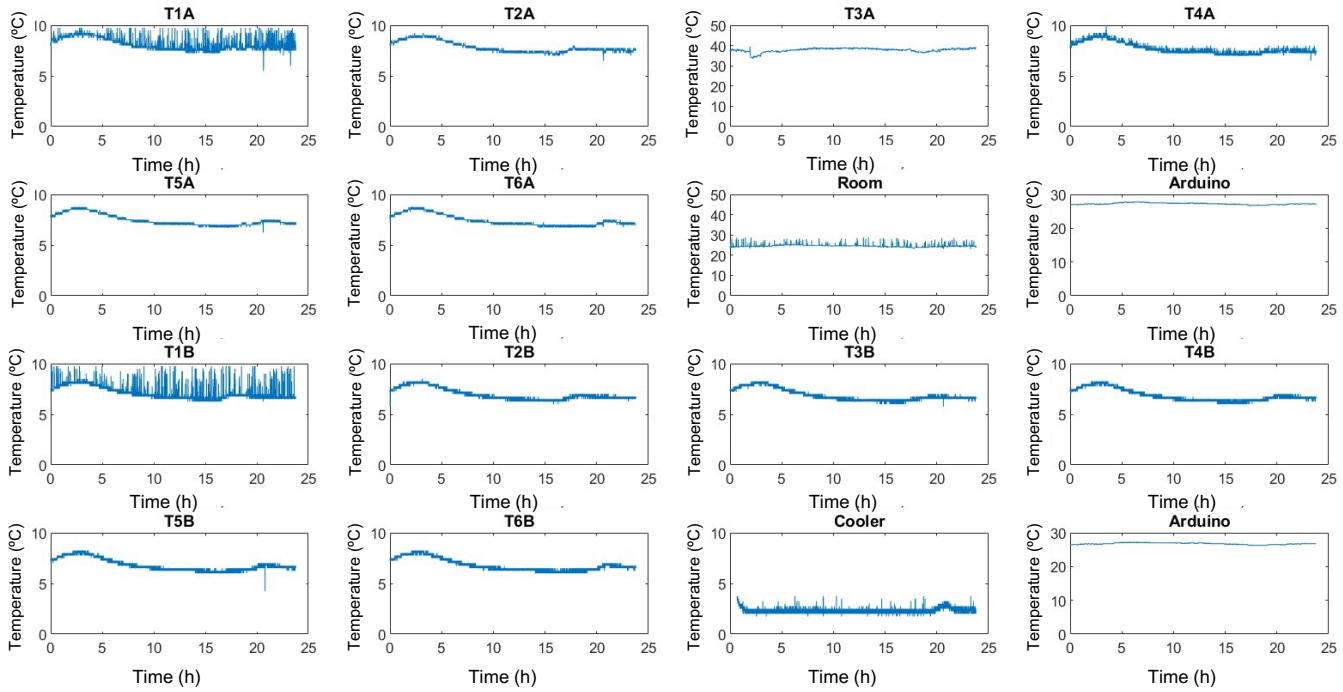


Figure 12. Temperature readings from 8 °C to 7 °C from the gas hydrate detection experimental procedure. Gas hydrate exothermic reaction was noticed after 17 h of cooling.

3.2. Small Diameter Core Sample Results

The coreflooding experiment with the smaller core sample equipped with highly accurate pressure gauges and a differential pressure transducer gives information about the saturation of gas hydrates and resulting permeability effects created under similar conditions as for the larger core sample described above.

To obtain the water permeability, pressure transducer differential measurements at water flow rates of 2, 1, and 0.5 mL/min were performed. The linear relation of differential pressure with flow rate shown in Figure 13 gives a positive slope of 0.4189 with a coefficient of determination equal to 1. With this relationship, the water permeability at flow rates below or above the possible measurements can be calculated through extrapolation. Because of the physical size of the smaller core sample, we reduced the injection rate to 0.05 mL/min to not reach water breakthrough too soon. At this flow rate, the pressure differential according to the relationship gives a value of 0.02080 psi resulting in a water permeability calculated according to Darcy's law (Equation (1)) with the physical dimensions of the smaller core sample of 1572.92 mD.

$$kw = \frac{q_{inj}\mu_w L}{A\Delta p} \quad (1)$$

At each of the temperatures following the cooling temperature ramp, pressure differential measurements were conducted and average values over the time of injection were calculated. The absolute permeability was calculated using Darcy's law at each of the temperature steps, and by relating these values to the water permeability, a relative hydrate permeability was calculated. Figure 14 plots the measured pressure differential and calculated relative hydrate permeability versus the respective temperature. The experiment started at a temperature of 15 °C. There was a slight decrease in the measured pressure differential from 15 to 8 °C, with a corresponding decrease in permeability. From 8 to 7 °C, there is a significant increase in the pressure differential, with a corresponding decrease in permeability, which coincides with the formation of solid hydrates within the pore space. Further decrease in temperature promoted the formation of more hydrate phase manifested by the increase in the measured pressure differential and decrease in permeability.

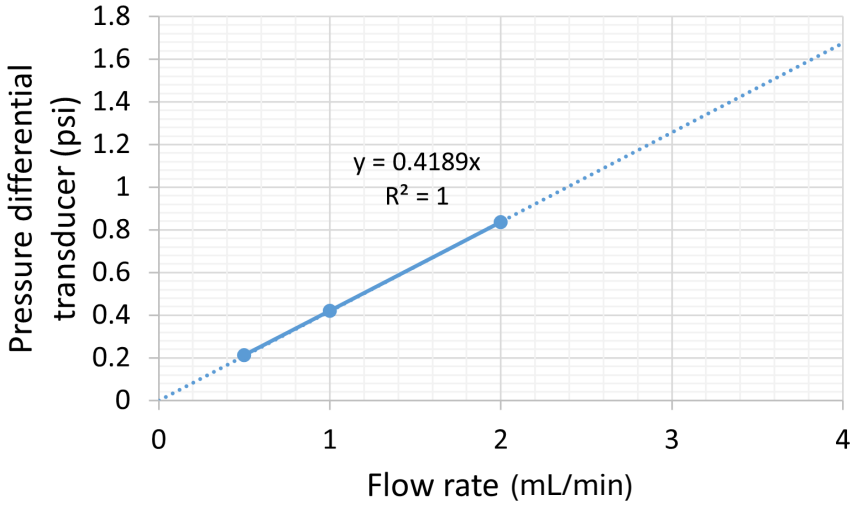


Figure 13. Pressure transducer differential measurements at water flow rates of 2, 1, and 0.5 mL/min including a linear trend line with a coefficient of determination of 1.

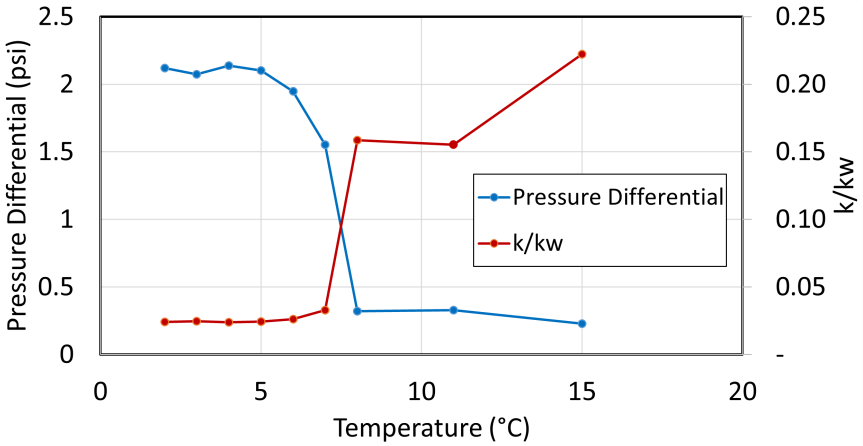


Figure 14. Measured pressure differential and relative hydrate permeability plotted against the temperature step in the cooling temperature ramp. A sudden increase in differential pressure manifesting in a steep drop of relative hydrate permeability at the hydrate forming temperature of 7 °C can be seen.

Different theoretical permeability models plotted in Figure 15 based on different hydrate deposition morphology show the relation of relative permeability with hydrate saturation. The models are either based on the idealistic mathematical assumption of the capillary bundle model or on the empirically derived relationship based on Kozeny-type equations. The derivation of both models for each of the two different hydrate formation deposition morphologies is summarized in Appendix A. Theoretical Permeability Models Derivation. Following our hypothesis of hydrate deposition in the center of the pores supported by the experiments on the large diameter core sample as described above, the hydrate saturation can be back-calculated with the theoretical models. Due to the non-linear relationship, this back-calculation was conducted using numerical methods. The results of this calculation are summarized in Table 3. The relative permeability was normalized to the 15 °C temperature step, where we have no hydrates and represents the baseline pressure differential. A normalized or corrected hydrate saturation was obtained using the theoretical models presented in Figure 15. A hydrate saturation as high as 38% is estimated for the temperature step of 2 ° C.

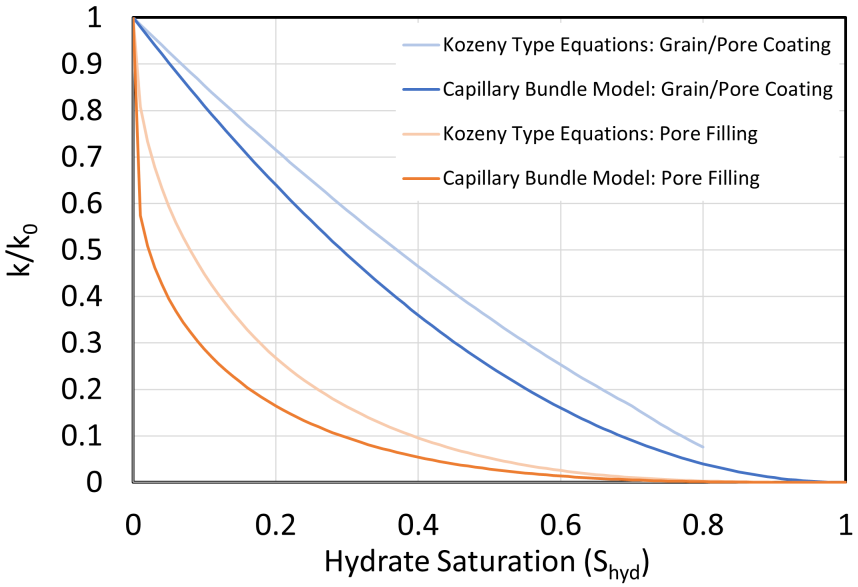


Figure 15. Theoretical permeability models based on the capillary bundle assumption and the Kozeny-type equations depending on the hydrate deposition morphology of pore filling and grain/pore coating. The equations yielding these models are derived in Appendix A. Theoretical Permeability Models Derivation.

Table 3. Calculated relative hydrate permeability based on Darcy's law with pressure differential measurements and resulting hydrate saturation based on the pore-filling deposition morphology according to the Kozeny-type equations.

Temperature (°C)	k/kw	k/kw Normalized	S_{hyd}	S_{hyd} Normalized
15	0.2222	1.0000	0.2417	0.0000
11	0.1553	0.6986	0.3135	0.0255
8	0.1586	0.7136	0.3093	0.0229
7	0.0328	0.1477	0.5670	0.3231
6	0.0262	0.1178	0.5959	0.3658
5	0.0243	0.1092	0.6052	0.3797
4	0.0239	0.1074	0.6072	0.3826
3	0.0246	0.1107	0.6036	0.3772
2	0.0240	0.1082	0.6063	0.3813

4. Future Work

The presented experimental procedures and results of gas hydrate formation in an undersaturated sandstone oil sample using multiphysics measurements delivers data for holistic numerical analyses and the development of a workflow to upscale the findings to the field-scale in the future. This will involve a numerical replication of the experimental procedures to match the observations from the laboratory coreflooding scale before the upscaling of virtual models can deliver predictions of gas hydrate formation in an oil reservoir that is subject to waterflooding. Furthermore, future work will include pore-scale modeling efforts to create a realistic distribution of gas hydrates in the porous media of a reservoir rock. This will be able to test the hydrate formation deposition morphology hypothesis and related permeability effects. Thereby, we would be able to validate idealistic theoretical permeability models with hydrate saturation using the actual pore structure in the framework of Digital Rock Physics modeling.

5. Conclusions

Gas hydrate formation at undersaturated oil reservoir conditions was detected through the coreflood experiments executed in this work. Gas hydrates formed during the 7 °C cool-

ing/injection step of the experimental procedure for the large diameter core sample. This initial gas hydrate formation was captured by P-waves and temperature measurements.

Strain measurements demonstrated that at 4 °C, the hydrate saturation was high enough to promote more significant changes in the interactions between rock and fluid. Additional hydrate formation at 4 °C promoted the expansion of the rock observed by the response of strain gauges.

Complex conductivity did not detect the initial gas hydrate formation because of the competition between the increase in electrical resistivity by solid hydrates and a decrease in electrical resistivity due to the increase in water salinity in remaining unconverted water.

From elastic wave analysis in the experiments, S-waves were not initially affected by the formation of gas hydrates, indicating a pore-filling morphology. This morphology has a greater permeability decrease than a pore-coating morphology, promoting the fluid flow resistance observed via pressure differential measurements between the inlet and outlet of the cores.

A highly accurate pressure differential transducer and the application of Darcy's law resulted in the calculation of the relative hydrate permeability which gave a theoretical quantification of the hydrate saturation by the assumption of the pore-filling deposition morphology based on Kozeny-type equations.

The findings of this research show a risk of performing waterflooding with cold seawater in shallow (colder) undersaturated oil reservoirs and give a method to estimate hydrate saturation and potential permeability decrease based on pressure measurements and theory.

Author Contributions: Conceptualization, L.E.Z. and M.P. (Manika Prasad); methodology, B.L.S.G., M.P. (Mathias Pohl), S.K., M.P. (Manika Prasad) and L.E.Z.; analysis, B.L.S.G., M.P. (Mathias Pohl), D.R., S.K. M.P. (Manika Prasad) and L.E.Z.; investigation, B.L.S.G., M.P. (Mathias Pohl), D.R., S.K., M.P. (Manika Prasad) and L.E.Z.; resources, L.E.Z.; writing—original draft preparation, B.L.S.G., D.R. and L.E.Z.; writing—review and editing, B.L.S.G., M.P. (Mathias Pohl), D.R., M.P. (Manika Prasad) and L.E.Z.; supervision, M.P. (Mathias Pohl), M.P. (Manika Prasad) and L.E.Z.; project administration, L.E.Z.; funding acquisition, M.P. (Manika Prasad) and L.E.Z. All authors have read and agreed to the published version of the manuscript.

Funding: This research was funded by OMV Norge AS, grant number 470121.

Data Availability Statement: The data that support the findings of this study are available on request from the corresponding author. The data are not publicly available due to privacy or ethical restrictions.

Acknowledgments: The authors would like to acknowledge Carolyn Koh, Ahmad Majid, Jyoti Behura, and Weiping Wang for the support through this research.

Conflicts of Interest: The authors declare no conflicts of interest.

Appendix A. Theoretical Permeability Model Derivation

In this paper, different models to relate relative gas hydrate permeability with hydrate saturation are presented. These models can be classified according to the hydrate deposition morphology hypothesis. Here, we show the derivation of the relative hydrate permeability as a function of hydrate saturation based on two main deposition morphologies: the grain/pore-coating morphology and the pore-filling morphology.

Appendix A.1. Capillary Bundle Model

The flux in a simple capillary bundle model consisting of n parallel and straight cylindrical capillaries is given by the Hagen-Poiseuille Equation (Equation (A1)) derived from the Navier-Stokes equations.

$$q = \frac{n\pi R^4}{8\mu}\frac{\Delta p}{L} \tag{A1}$$

where q is the flux in m^3/s, n is the number of capillaries, R is the radius of the capillaries in m, Δp is the pressure differential in Pa, μ is the viscosity in Pa.s, and L is the length of the capillaries in m.

Combining this equation with the flux calculated based on Darcy's law (Equation (1)) gives the permeability as

$$k = \frac{n\pi R^4}{8} \tag{A2}$$

Relating that to the porosity definition in the capillary bundle model of $\phi = n\pi R^2$, the permeability without hydrates becomes

$$k_0 = \frac{\phi R^2}{8} \tag{A3}$$

Appendix A.1.1. Grain/Pore-Coating Morphology

A uniform coating of the walls around the capillaries reduces the radius of the capillaries to R_1 and the permeability becomes

$$k_1 = \frac{n\pi R_1^4}{8} \tag{A4}$$

According to the definition of the porosity, the number of capillaries remain the same with

$$n = \frac{\phi}{\pi R^2} \tag{A5}$$

Inserting (Equation (A5)) in (Equation (A4)) yields the reduction in permeability due to the coating of hydrates, as follows:

$$k_1 = \frac{\frac{\phi}{R^2} R_1^4}{8} = \frac{\phi R_1^4}{8R^2} \tag{A6}$$

The reduced radius can be written as a function of the original radius in terms of the hydrate saturation as reducing fraction such as $R_1^2 = R^2 * (1 - S_h)$, resulting in

$$k_1 = \frac{\phi R^4 (1 - S_h)^2}{8R^2} = \frac{\phi R^2 (1 - S_h)^2}{8} \tag{A7}$$

The relative hydrate permeability is defined as the ratio of the reduced permeability due to hydrates to the original one without hydrates and can be expressed by combining (Equation (A7)) with (Equation (A3)), as follows:

$$\frac{k_1}{k_0} = \frac{\frac{\phi R^2 (1-S_h)^2}{8}}{\frac{\phi R^2}{8}} = (1 - S_h)^2 \tag{A8}$$

Appendix A.1.2. Pore-Filling Morphology

Assuming that hydrates form in the center of the capillaries creating a cylinder within a cylinder, the annular flux of a single capillary is [25]

$$q = \frac{\pi}{8\mu} \frac{\Delta p}{L} (R^4 - R_1^4 - \frac{(R^2 - R_1^2)^2}{log(\frac{R}{R_1})}) \tag{A9}$$

where R is the radius of the capillary cylinder and R_1 is the radius of the hydrate cylinder.

Combining this expression with Darcy's flux (Equation (1)) and multiplying it with n for a bundle of capillaries gives the absolute permeability as

$$k = \frac{n\pi}{8} (R^4 - R_1^4 - \frac{(R^2 - R_1^2)^2}{log(\frac{R}{R_1})}) \tag{A10}$$

Dividing both sides by R^4 results in a better mathematical expression for later on, as follows:

$$k = \frac{n\pi R^4}{8}(1 - \frac{R_1^4}{R^4} - \frac{(1 - \frac{R_1^2}{R^2})^2}{log(\frac{R}{R_1})}) \tag{A11}$$

The hydrate saturation as percentage of the total pore volume assuming cylindrical shapes can be written as

$$S_h = \frac{2\pi L R_1^2}{2\pi L R^2} = \frac{R_1^2}{R^2} \tag{A12}$$

This gives the permeability as a function of the hydrate saturation by combining (Equation (A12)) with (Equation (A11)), as follows:

$$k_1 = \frac{n\pi R^4}{8}(1 - S_h^2 - \frac{(1 - S_h)^2}{log(\sqrt{\frac{1}{S_h}})}) \tag{A13}$$

To include the porosity with the definition of n (Equation (A5)), the final form for the hydrate permeability becomes

$$k_1 = \frac{\phi R^2}{8}(1 - S_h^2 - \frac{(1 - S_h)^2}{log(\sqrt{\frac{1}{S_h}})}) \tag{A14}$$

Following the approach to relate (Equation (A14)) with (Equation (A3)) to each other, the relative hydrate permeability in the pore-filling morphology becomes

$$\frac{k_1}{k_0} = \frac{\frac{\phi R^2}{8}(1 - S_h^2 - \frac{(1-S_h)^2}{log(\sqrt{\frac{1}{S_h}})})}{\frac{\phi R^2}{8}} = 1 - S_h^2 - \frac{(1 - S_h)^2}{log(\sqrt{\frac{1}{S_h}})} \tag{A15}$$

Appendix A.2. Kozeny-Type Equation

Due to the irregular shape of pores and flow paths that results usually in a greater length than a straight path, the Kozeny family of hydraulic permeability introduces shape factors and tortuosity [26], as follows:

$$k = \frac{\phi}{\nu\tau(\frac{A}{V})^2_{pore}} \tag{A16}$$

where ν is the shape factor and τ is the tortuosity defined as

$$\tau = (\frac{L_1}{L_0})^2 \tag{A17}$$

The tortuosity is also related to the electrical formation factor F and the porosity with $\tau = F\phi$ [27].

Assuming that only the area, pore volume, and electrical formation factor change, and the shape factor ν stays constant with the formation of hydrates, the relative permeability becomes then by relating

$$\frac{k_1}{k_0} = \frac{\frac{\phi}{\nu F_1 \phi(\frac{A_1}{V_1})^2}}{\frac{\phi}{\nu F_0 \phi(\frac{A_0}{V_0})^2}} = \frac{F_0}{F_1}(\frac{A_0 V_1}{A_1 V0})^2 \tag{A18}$$

The formation factor change between hydrate saturation F_1 and water saturation F_0 can be described with the hydrate saturation and Archie's exponent n [28] such that

$$\frac{F_1}{F_0} = (1 - S_h)^{-n} \tag{A19}$$

Now, the relative permeability depends only on the surface area ratio depending on the morphological model assumption, as follows:

$$\frac{k_1}{k_0} = (1 - S_h)^{n+2}(\frac{A_0}{A_1})^2 \tag{A20}$$

Appendix A.2.1. Grain/Pore-Coating Morphology

In the morphological assumption of hydrates coating the grains, the surface area decreases with increasing hydrate saturation, as follows:

$$\frac{A_0}{A_1} = \frac{2\pi LR}{2\pi LR_1} = \frac{R}{R_1} \tag{A21}$$

As the volume of a cylinder is $V = 2\pi LR^2$, the surface area relation as a function of the hydrate saturation becomes

$$S_h = \frac{V_1}{V_0} = \frac{2\pi L(R^2 - R_1^2)}{2\pi LR^2} = 1 - \frac{R_1^2}{R^2} \tag{A22}$$

Rearranging the equation then gives

$$(1 - S_h) = \frac{R_1^2}{R^2} \tag{A23}$$

Furthermore, combining (Equation (A23)) with (Equation (A21)) yields

$$\frac{A_0}{A_1} = \frac{1}{\sqrt{1 - S_h}} \tag{A24}$$

This gives the relative hydrate permeability as a function of the hydrate saturation resulting in

$$\frac{k_1}{k_0} = (1 - S_h)^{n+2}\frac{1}{1 - S_h} = (1 - S_h)^{n+1} \tag{A25}$$

According to [28], Archie's saturation exponent n equals 1.5 for $0 < S_h < 0.8$ with a diverging value at a hydrate saturation greater than 80%.

Appendix A.2.2. Pore-Filling Morphology

As hydrates grow in the center of the capillary, the surface area grows as well according to (Equation (A21)).

The hydrate saturation is related to the volume of the capillaries with

$$S_h = \frac{V_1}{V_0} = \frac{2\pi LR_1^2}{2\pi L(R - R_1)^2} = \frac{R_1^2}{R^2 - R_1^2} = \frac{R_1^2}{R^2} - 1 \tag{A26}$$

$$\frac{R_1}{R} = \sqrt{S_h} + 1 \tag{A27}$$

Combining (Equation (A21)) with (Equation (A27)) gives

$$\frac{A_0}{A_1} = \frac{1}{1 + \sqrt{S_h}} \tag{A28}$$

Then, the relative hydrate permeability is expressed as

$$\frac{k_1}{k_0} = (1 - S_h)^{n+2}(\frac{1}{1 + \sqrt{S_h}})^2 = \frac{(1 - S_h)^{n+2}}{(1 + \sqrt{S_h})^2} \tag{A29}$$

According to [28], the n exponent increases approximately linearly from $n = 0.4$ at $S_h = 0.1$ to $n = 1$ at $S_h = 1$ yielding the linear dependency of $n(S_h) = \frac{2}{3} * S_h + \frac{1}{3}$.

References

1. Sloan, E.D. Introductory Overview: Hydrate Knowledge Development. *Am. Mineral.* **2004**, *89*, 1155–1161. [CrossRef]
2. Sloan, E.D.; Koh, C.A. *Clathrate Hydrates of Natural Gases*; CRC Press: Boca Raton, FL, USA, 2007.
3. Holder, G.D.; Katz, D.L.; Hand, J.H. Hydrate Formation in Subsurface Environments. *AAPG Bull.* **1976**, *60*, 981–988.
4. Verma, V.K.; Hand, J.H.; Katz, D.L. Gas Hydrates from Liquid Hydrocarbons (Methane-Propane-Water System). In Proceedings of the GVC/AIChE Joint Meeting, Munich, Germany, 17–20 September 1974.
5. Kumar, A.; Maini, B.B.; Bishnoi, P.R.; Clarke, M.; Zatsepina, O.; Srinivasan, S. Experimental Determination of Permeability in the Presence of Hydrates and its Effect on the Dissociation Characteristics of Gas Hydrates in Porous Media. *J. Pet. Sci. Eng.* **2010**, *70*, 114–122. [CrossRef]
6. Delli, M.L.; Grozic, J.L.H. Experimental Determination of Permeability of Porous Media in the Presence of Gas Hydrates. *J. Pet. Sci. Eng.* **2014**, *120*, 1–9. [CrossRef]
7. Johnson, A.; Patil, S.; Dandekar, A. Experimental Investigation of Gas-Water Relative Permeability for Gas-Hydrate-Bearing Sediments from the Mount Elbert Gas Hydrate Stratigraphic Test Well, Alaska North Slope. *Mar. Pet. Geol.* **2011**, *28*, 419–426. [CrossRef]
8. Nimblett, J.; Ruppel, C.D. Permeability Evolution During the Formation of Gas Hydrates in Marine Sediments. *J. Geophys. Res. Solid Earth* **2003**, *108*, 2420–2467. [CrossRef]
9. Liu, X.; Flemings, P.B. Dynamic Multiphase Flow Model of Hydrate Formation in Marine Sediments. *J. Geophys. Res. Solid Earth* **2007**, *112*, 3101–3132. [CrossRef]
10. Waite, W.F.; Santamarina, J.C.; Cortes, D.D.; Dugan, B.; Espinoza, D.N.; Germaine, J.; Jang, J.; Jung, J.W.; Kneafsey, T.J.; Shin, H.; et al. Physical Properties of Hydrate-Bearing Sediments. *Rev. Geophys.* **2009**, *47*, 4003–4041. [CrossRef]
11. Dai, S.; Santamarina, J.C.; Waite, W.F.; Kneafsey, T.J. Hydrate Morphology: Physical Properties of Sands with Patchy Hydrate Saturation. *J. Geophys. Res. Solid Earth* **2012**, *117*, B11205. [CrossRef]
12. Ecker, C.; Dvorkin, J.; Nur, A. Sediments with gas hydrates: Internal structure from seismic AVO. *Geophysics* **1998**, *63*, 1659–1669. [CrossRef]
13. Priegnitz, M.; Thaler, J.; Spangenberg, E.; Schicks, J.M.S.; Schrötter, J.; Abendroth, S. Characterizing Electrical Properties and Permeability Changes of Hydrate Bearing Sediments Using ERT Data. *Geophys. J. Int.* **2015**, *202*, 1599–1612. [CrossRef]
14. Hyndman, R.D.; Spence, G.D. A Seismic Study of Methane Hydrate Marine Bottom Simulating Reflectors. *J. Geophys. Res. Solid Earth* **1992**, *97*, 6683–6698. [CrossRef]
15. Katzman, R.; Holbrook, W.S.; Paull, C.K. Combined Vertical-Incidence and Wide-Angle Seismic Study of a Gas Hydrate Zone, Blake Ridge. *J. Geophys. Res. Solid Earth* **1994**, *99*, 17975–17995. [CrossRef]
16. Sahoo, S.K.; Madhusudhan, B.N.; Marín-Moreno, H.; North, L.J.; Ahmed, S.; Falcon-Suarez, I.H.; Minshull, T.A.; Best, A.I. Laboratory Insights Into the Effect of Sediment-Hosted Methane Hydrate Morphology on Elastic Wave Velocity From Time-Lapse 4-D Synchrotron X-Ray Computed Tomography. *Geochem. Geophys. Geosyst.* **2018**, *19*, 4502–4521. [CrossRef]
17. Singh, S.C.; Minshull, T.A.; Spence, G.D. Velocity Structure of a Gas Hydrate Reflector. *Science* **1993**, *260*, 204–207. [CrossRef]
18. Edwards, R.N. On the Resource Evaluation of Marine Gas Hydrate Deposits Using Sea-floor Transient Electric Dipole-dipole Methods. *Geophysics* **1997**, *62*, 63–74. [CrossRef]
19. Du Frane, W.L.; Stern, L.A.; Weitemeyer, K.A.; Constable, S.; Pinkston, J.C.; Roberts, J.J. Electrical Properties of Polycrystalline Methane Hydrate. *Geophys. Res. Lett.* **2011**, *38*, L09313. [CrossRef]
20. Du Frane, W.L.; Stern, L.A.; Constable, S.; Weitemeyer, K.A.; Smith, M.M.; Roberts, J.J. Electrical Properties of Methane Hydrate+ Sediment Mixtures. *J. Geophys. Res. Solid Earth* **2015**, *120*, 4773–4783. [CrossRef]
21. Yuan, J.; Edwards, R. The Assessment of Marine Gas Hydrates through Electrical Remote Sounding: Hydrate Without a BSR? *Geophys. Res. Lett.* **2000**, *27*, 2397–2400. [CrossRef]
22. Pohl, M. Ultrasonic and Electrical Properties of Hydrate-Bearing Sediments. Ph.D. Thesis, Colorado School of Mines, Golden, CO, USA, 2018.
23. Peksa, A.E.; Wolf, K.H.A.A.; Zitha, P.L.J. Bentheimer Sandstone Revisited for Experimental Purposes. *Mar. Pet. Geol.* **2015**, *67*, 701–719. [CrossRef]
24. Geranutti, B.L.S. Investigation of Gas Hydrate Formation during Sea Water Injection Based on Undersaturated Oil Core Flooding Experiments. Master's Thesis, Colorado School of Mines, Golden, CO, USA, 2020.
25. Lamb, H. *Hydrodynamics*; Dover: Mineola, NY, USA, 1945; pp. 331–332.
26. Scheidegger, A.E. *The Physics of Flow through Porous Media*; Macmillan: Old Tappan, NJ, USA, 1960.
27. Hearst, J.R.; Nelson, P.H.; Paillet, F.L. *Well Logging for Physical Properties*; McGraw-Hill: New York, NY, USA, 2000.
28. Spangenberg, E. Modeling of the Influence of Gas Hydrate Content on the Electrical Properties of Porous Sediments. *J. Geophys. Res.* **2001**, *106*, 6535–6548. [CrossRef]

Disclaimer/Publisher's Note: The statements, opinions and data contained in all publications are solely those of the individual author(s) and contributor(s) and not of MDPI and/or the editor(s). MDPI and/or the editor(s) disclaim responsibility for any injury to people or property resulting from any ideas, methods, instructions or products referred to in the content.